

Magnetic properties of $\text{GdT}_2\text{Zn}_{20}$ ($T = \text{Fe, Co}$) investigated by x-ray diffraction and spectroscopyJ. R. L. Mardegan,^{1,2} S. Francoual,² G. Fabbri,^{3,4,5} L. S. I. Veiga,² J. Stremper,² D. Haskel,³ R. A. Ribeiro,⁶ M. A. Avila,⁶ and C. Giles¹¹*Instituto de Física “Gleb Wataghin”, Universidade Estadual de Campinas, Campinas, São Paulo 13083-859, Brazil*²*Deutsches Elektronen-Synchrotron (DESY), Hamburg 22607, Germany*³*Advanced Photon Source, Argonne National Laboratory, Argonne, Illinois 60439, USA*⁴*Department of Physics, Washington University, St. Louis, Missouri 63130, USA*⁵*Department of Condensed Matter Physics and Materials Science, Brookhaven National Laboratory, Upton, New York 11973, USA*⁶*CCNH, Universidade Federal do ABC (UFABC), Santo André, São Paulo 09210-580, Brazil*

(Received 29 August 2015; revised manuscript received 16 November 2015; published 26 January 2016)

We investigate the magnetic and electronic properties of the $\text{GdT}_2\text{Zn}_{20}$ ($T = \text{Fe}$ and Co) compounds using x-ray resonant magnetic scattering (XRMS), x-ray absorption near-edge structure (XANES), and x-ray magnetic circular dichroism (XMCD). The XRMS measurements reveal that $\text{GdCo}_2\text{Zn}_{20}$ has a commensurate antiferromagnetic spin structure with a magnetic propagation vector $\vec{\tau} = (\frac{1}{2}, \frac{1}{2}, \frac{1}{2})$ below the Néel temperature ($T_N \sim 5.7$ K). Only the Gd ions carry a magnetic moment forming an antiferromagnetic structure with magnetic representation Γ_6 . For the ferromagnetic $\text{GdFe}_2\text{Zn}_{20}$ compound, an extensive investigation was performed at low temperature and under magnetic field using XANES and XMCD. A strong XMCD signal of about 12.5% and 9.7% is observed below the Curie temperature ($T_C \sim 85$ K) at the Gd L_2 and L_3 edges, respectively. In addition, a small magnetic signal of about 0.06% of the jump is recorded at the Zn K edge, suggesting that the Zn $4p$ states are spin polarized by the Gd $5d$ extended orbitals.

DOI: [10.1103/PhysRevB.93.024421](https://doi.org/10.1103/PhysRevB.93.024421)**I. INTRODUCTION**

The demand for new materials with interesting and useful physical properties has led to the fast development in material science. Properties such as superconductivity, magnetic ordering, and nearly ferromagnetic Fermi-liquid and heavy fermion behavior have been observed in many materials, including the family of complex intermetallic compounds $RT_2\text{Zn}_{20}$ ($R = \text{rare earth}$, $T = \text{transition metal}$) [1–5]. This family, first reported two decades ago by Nasch *et al.* [6], has been extensively used as a model system due to its rather unique structure, which features a complex but well-ordered crystal structure. The $RT_2\text{Zn}_{20}$ compounds have a cubic structure with $Fd\bar{3}m$ (No. 227) space group in which the R and T ions occupy the crystallographic sites $8a$ and $16d$, respectively. Moreover, these ions are each encapsulated in quasispherical cages formed exclusively by Zn ions, which occupy three inequivalent Wyckoff positions given by $16c$, $48f$, and $96g$, as can be viewed in Fig. 1. Two particular properties observed in these materials have attracted great attention: a remarkably high magnetic ordering temperature observed in the $R\text{Fe}_2\text{Zn}_{20}$ series (although it contains less than 5% of R ion) and a nearly ferromagnetic Fermi-liquid behavior in $\text{YFe}_2\text{Zn}_{20}$ [2,4].

In several studies it has been argued, based on macroscopic measurements and band structure calculations, that the elevated magnetic ordering temperatures and the type of magnetic ordering are attributed to a high density of states (DOS) at the Fermi level [2–4,7–9]. For instance, the Co-based compounds $\text{GdCo}_2\text{Zn}_{20}$ and $\text{TbCo}_2\text{Zn}_{20}$ present an antiferromagnetic (AFM) ordering below ~ 5.7 K and 2.5 K, respectively, in which the larger R – R distance (~ 6 Å) supports an indirect interaction and a low transition temperature. When the Co ions are replaced by Fe ions ($\text{GdFe}_2\text{Zn}_{20}$ and $\text{TbFe}_2\text{Zn}_{20}$), the compounds exhibit ferromagnetic (FM) ordering with the transition temperatures drastically raised to 86 and 66 K,

respectively. The relatively long distance between rare-earth ions in the structure weakens the Ruderman-Kittel-Kasuya-Yosida (RKKY) exchange interaction, while the high density of Fe $3d$ bands at the Fermi level directly affects the conduction electrons.

Recently, a detailed study of the magnetic structure of $\text{TbCo}_2\text{Zn}_{20}$ and $\text{TbFe}_2\text{Zn}_{20}$ using magnetic neutron scattering at low temperature was reported [7]. Although the Tb-based compounds present similar magnetic properties as compared to $\text{GdCo}_2\text{Zn}_{20}$ and $\text{GdFe}_2\text{Zn}_{20}$, the absence of crystalline electric field (CEF) at first order and a strong RKKY interaction in the Gd compounds affect the electronic and magnetic interactions between the rare-earth ions and the surrounding matrix. In particular, the investigation of the compounds with a half-filled $4f^7$ shell (Gd-based materials) at low temperature can provide information about the physical properties and these compounds are very important as reference compounds due to their lack of orbital momentum, i.e., $S = 7/2$ and $L = 0$, which leads to magnetic properties that are unaffected by spin-orbit coupling. In order to understand the implications of such interactions, we have used spectroscopy and magnetic scattering techniques to probe in detail the electronic and magnetic properties of the $\text{GdT}_2\text{Zn}_{20}$ family. Due to the large Gd neutron absorption cross section, x-rays are the ideal alternative to probe the magnetic and electronic properties in these materials. Furthermore, the incoming beam energy can be tuned to the absorption edge, thus providing chemical and atomic selectivity, i.e., the magnetic response of each element can be probed separately.

Here we report the magnetic and electronic structure at low temperature of the $\text{GdT}_2\text{Zn}_{20}$ ($T = \text{Fe, Co}$) compounds using the x-ray resonant magnetic scattering (XRMS), x-ray absorption near-edge structure (XANES), and x-ray magnetic circular dichroism (XMCD) techniques. The XRMS measurements performed on $\text{GdCo}_2\text{Zn}_{20}$ reveal a commensurate

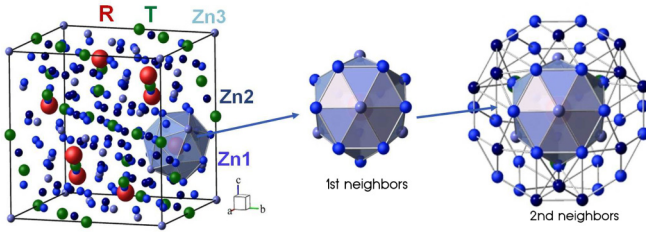


FIG. 1. RT_2Zn_{20} structural representation. The Zn ions are shown at the three sites (Zn1–Zn3) and the Zn cages are shown in detail in which there is a R atom inside.

antiferromagnetic ordering with a magnetic propagation vector $\vec{\tau} = (\frac{1}{2}, \frac{1}{2}, \frac{1}{2})$ below $T_N = 5.72(6)$ K. In addition, at low temperature, the Gd magnetic moments order following the magnetic representation Γ_6 in which the magnetic moment direction is written as a linear combination of the two basis vectors ψ_5 and ψ_6 . This magnetic structure is consistent with a $P5_1$ magnetic space group. The XMCD measurements performed below the Curie temperature [$T_C = 85(2)$ K] in $GdFe_2Zn_{20}$ display a dichroic signal of 12.5% and 9.7% of the absorption jump for Gd L_2 and L_3 edges, respectively. Surprisingly, a magnetic signal of about 0.06% is detected at the Zn K edge, which suggests that the Zn ions are spin polarized. This magnetic signal might originate from the hybridization between the extended Gd $5d$ bands with the empty Zn $4sp$ states. Absorption measurements performed at the Fe K edge do not reveal any magnetic contribution coming from the iron ions above the background level.

II. EXPERIMENTAL DETAILS

High-quality single crystals of $GdFe_2Zn_{20}$ and $GdCo_2Zn_{20}$ were grown at the Universidade Federal do ABC by the Zn self-flux method [10,11], similar to that reported in previous studies on the family [2–4]. In order to perform the absorption measurements at the Gd $L_{2,3}$, Fe and Zn K edge, selected single crystals of $GdFe_2Zn_{20}$ were ground and sieved, resulting in fine powders with grain sizes around 3 – 5 μm . The magnetic diffraction measurements were done on a high-quality $GdCo_2Zn_{20}$ single crystal cut to dimensions of approximately $2 \times 2 \times 0.5$ mm^3 . The crystalline piece was carefully polished to achieve a flat surface perpendicular to the [111] direction, yielding a mosaic width of approximately 0.02° . The phase purity of the samples was confirmed by powder diffraction using conventional laboratory x-ray sources. Temperature-dependent magnetic susceptibility measurements (not shown here) were performed using a commercial superconducting quantum interference device (Quantum Design MPMS-SQUID) to verify the magnetic ordering temperatures, the effective magnetic moments, and the Curie-Weiss constants.

The resonant diffraction measurements were performed at beamline 6-ID-B at the Advanced Photon Source (APS), Argonne National Laboratory, whereas the absorption measurements were conducted at 4-ID-D (APS) [12] and at beamline P09 at PETRA III (DESY) [13].

A. Absorption experiment

XANES and XMCD spectra obtained at low temperature for the Gd $L_{2,3}$, Fe and Zn K -absorption edges were performed in transmission geometry on powdered $GdFe_2Zn_{20}$ samples. The samples were cooled down by a displax cryostat with base temperature around 7 K. XMCD spectra were performed in helicity switching mode in which the left and right circular polarization was obtained by means of diamond phase plates [14]. The degree of circularly polarized beam was higher than 95% for both beamlines (P09 and 4-ID-D) [15,16]. An external magnetic field of $H = 2.0$ T (at APS) and 0.8 T (at DESY) was applied in the $GdFe_2Zn_{20}$ samples along and opposite to the incident beam wave vector \hat{k} to align the ferromagnetic domains and to correct for nonmagnetic artifacts in the XMCD data. Those external magnetic fields were enough to reach the saturation magnetization according to the macroscopic measurements.

B. Scattering experiment

XRMS measurements were performed at $T = 4.5$ K on $GdCo_2Zn_{20}$ single crystal, mounted inside the closed-cycle displax cryostat in a six-circle diffractometer at the 6-ID-B beam line. The single crystal was oriented with the [111] direction parallel to the vertical diffraction plane. Several magnetic superlattice reflections of the type $(\frac{L}{2}, \frac{L}{2}, \frac{L}{2})$ with $L = (2n + 1)$ were measured and their integrated intensities were compared to the simulated intensities to determine the magnetic structure below T_N . To enhance the magnetic Bragg peak intensities, the energy of the incident beam was tuned near the Gd L_2 or L_3 absorption edges. In addition, in order to investigate any magnetic contribution from Co and Zn ions, the energy of the incident beam was also tuned to the Co (7709 eV) and Zn (9659 eV) K edges and a search for superlattice reflections was performed. The charge and magnetic contributions present in the scattered beam were separated by a pyrolytic graphite [C(006)] analyzer crystal installed on the 2θ arm of the diffractometer. Since the incident beam presents the polarization perpendicular to the diffraction plane (σ polarization), by rotation of the analyzer crystal around the scattered beam wave vector \vec{k}' , we were able to select the two polarization channels ($\sigma - \sigma'$ and $\sigma - \pi'$) in this experimental geometry [17].

III. EXPERIMENTAL RESULTS

The experimental results are organized into two sections. The first part is dedicated to the absorption measurements on powdered $GdFe_2Zn_{20}$ in its FM state. The subsequent section shows the results obtained by the XRMS technique on the $GdCo_2Zn_{20}$ single crystal in its AFM state.

A. Absorption measurements: $GdFe_2Zn_{20}$

XANES and XMCD measurements performed at the Gd $L_{2,3}$ edges in $GdFe_2Zn_{20}$ are shown in Fig. 2. Dipolar selection rules make the dichroic signal at the $L_{2,3}$ absorption edges sensitive to the spin polarization of the intermediate $5d$ level. The Gd XANES reported in Fig. 2 are normalized to one at the L_3 and half at the L_2 edge to reflect the 2:1 ratio of

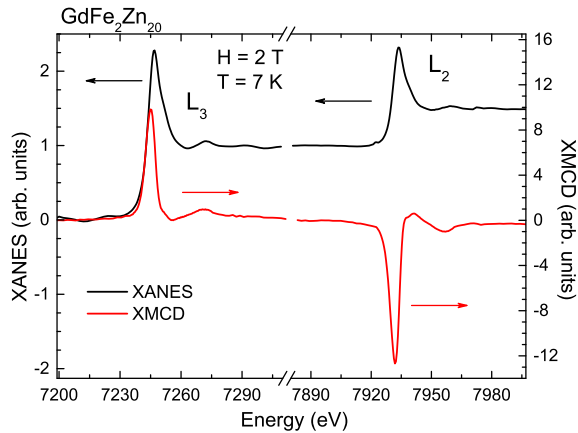


FIG. 2. XANES and XMCD spectra obtained at the Gd $L_{2,3}$ edges performed at $T = 7$ K and $H = 2$ T.

the initial state at these edges ($2p_{3/2}$ and $2p_{1/2}$, respectively). Figure 2 also shows the XMCD spectra at the Gd $L_{2,3}$ edges in which each spectrum is normalized to the corresponding edge jump of the absorption spectrum. The XMCD signal obtained across the two edges shows different intensities, with a strong dichroic magnetic signal around 12.5% at the L_2 and 9.7% at the L_3 absorption edges, which is consistent with Gd-based compounds [18].

The size and the shape of the magnetic contribution obtained by fitting the XMCD signals with the Lorentzian function can describe additional properties of this system. The widths of the dipolar (E1) contributions observed at the L_2 and L_3 absorption edges are 4.3(2) and 4.5(2) eV, respectively, which reflects a short $2p$ core hole lifetime. Using the integrated intensities, the L_3/L_2 ratio (or branching ratio value, BR) [19–23] obtained experimentally is $-0.77(4)$.

Absorption measurements at the Fe and Zn K edges were also carried out on powdered samples. The absorption measurement near the K edge, in which the dipolar transition is probed ($1s \rightarrow 4p$), is crucial to understand the magnetic and electronic properties due to the delocalized character of the p states [24]. Since the probed p states are very delocalized, a strong influence of the surrounding matrix can be expected due to the hybridization between the rare-earth and the transition-metal ions. As shown in Fig. 3, the measurements performed near the Fe K edge do not reveal any magnetic contribution from the Fe ions higher than the background level ($\sim 0.07\%$). The inset in Fig. 3 exhibits the XMCD measurements obtained for a $5 \mu\text{m}$ Fe foil in the same experimental conditions: a clear dichroic signal can be observed near the edge.

However, the spectroscopy measurement at the Zn K edge manifests an interesting behavior. Figure 4 shows the absorption and dichroism results at the Zn K edge in which an induced magnetic signal around 0.06% is detected. This magnetic signal is due to a hybridization with the rare-earth $5d$ orbitals. The XMCD spectrum exhibits the main positive feature located at 9665 eV with a width around 2.5 eV, surrounded by two negative peaks 6.5 eV away. The broad feature localized around 9680 eV (~ 20 eV above the edge) is likely due to magnetic extended x-ray absorption fine structure (EXAFS) [25].

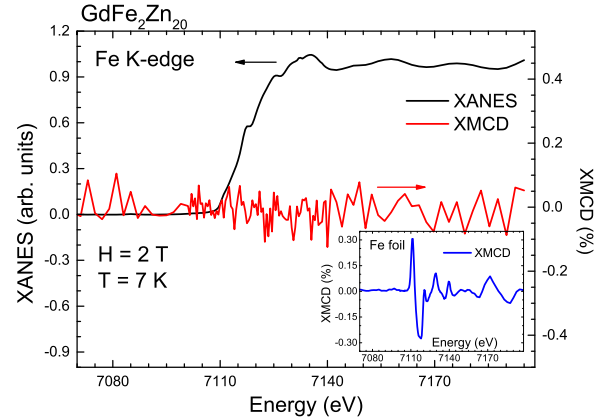


FIG. 3. X-ray absorption measurements at 7 K and in 2 T at the Fe K -absorption edge for $\text{GdFe}_2\text{Zn}_{20}$. The inset shows the XMCD data for the Fe-foil sample.

A clear evidence of the Zn $4p$ state's polarization due to the Gd ions can be found in the temperature and field dependence reported in Figs. 5(a) and 5(b), respectively. The magnetic intensities for both Gd and Zn ions follow the same temperature evolution and disappear around the critical temperature ($T_C \sim 85$ K). In addition, the two hysteresis loops obtained at the maximum XMCD intensity show clearly the Zn magnetism dependence in relation to the Gd ions and therefore it suggests a spin polarization of the Zn $4p$ bands by the Gd sublattice.

B. Magnetic scattering measurements: $\text{GdCo}_2\text{Zn}_{20}$

Figure 6 shows the evolution of the integrated intensity for the magnetic Bragg reflection ($\frac{7}{2}, \frac{7}{2}, \frac{3}{2}$) as a function of temperature for the $\text{GdCo}_2\text{Zn}_{20}$ compound fitted by a Lorentzian-squared function. The magnetic peak intensity decreases smoothly to zero as the temperature approaches T_N , indicating a standard second-order phase transition from an AFM to a paramagnetic state. The dashed red line in Fig. 6 displays a fitting using a critical power-law expression, $(1 - T/T_N)^{2\beta}$, above 5.0 K. The fitting around the Néel temperature yields $T_N = 5.72(6)$ K and a critical exponent $\beta = 0.36(3)$. The value of T_N is in good agreement with bulk magnetic susceptibility measurements and previous studies

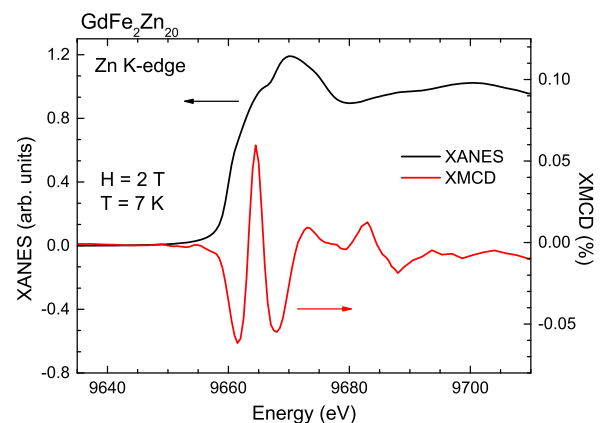


FIG. 4. X-ray absorption measurements at 7 K and in 2 T for the Zn K -absorption edge.

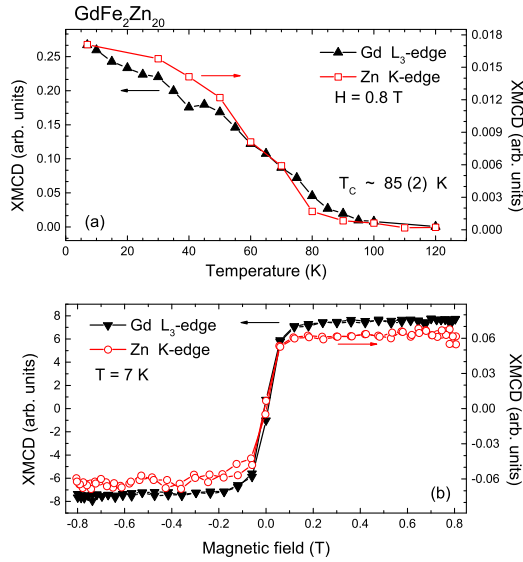


FIG. 5. (a) Temperature dependence and (b) XMCD hysteresis loops obtained at the Gd L_3 and Zn K -absorption edges.

[3,4]. The critical exponent β close to 0.367 suggests a three-dimensional (3D) Heisenberg magnetic model [26,27]. The blue square symbol in Fig. 6 reports the full width at half maximum (FWHM) of the magnetic superlattice peak $(\frac{7}{2}, \frac{7}{2}, \frac{3}{2})$ as a function of temperature. This figure clearly shows a peak broadening and a decrease in intensity near the phase-transition temperature characteristic of a loss of long-range order. The width of the magnetic Bragg peak is inversely proportional to the correlation length (ξ). From the FWHM data, the estimated correlation length at low temperature is $\xi \sim 1100 \text{ \AA}$.

Energy dependences across the Gd L_2 and L_3 edges performed at 4.5 K are displayed in Fig. 7. Figures 7(a) and 7(c) show the normalized absorption coefficients (μ) obtained from the fluorescence yield, while Figs. 7(b) and 7(d) exhibit the energy profile obtained at the magnetic superlattice position $(\frac{7}{2}, \frac{7}{2}, \frac{7}{2})$ with the analyzer crystal set to the $\sigma - \pi'$ polarization channel. A resonant enhancement of over two orders of magnitude at both absorption edges can be seen. In

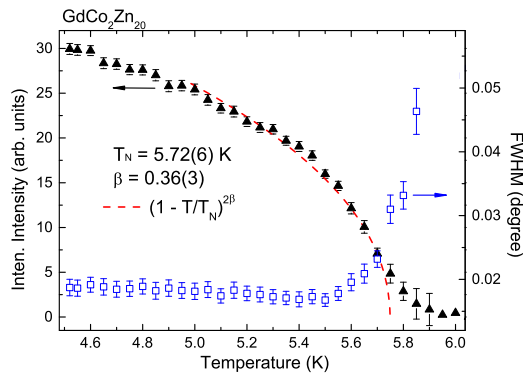


FIG. 6. Temperature dependence of the integrated intensity measured with a rocking scan through the superlattice peak $(\frac{7}{2}, \frac{7}{2}, \frac{3}{2})$. The inset shows T_N and the critical exponent β obtained from a critical power-law fitting $(1 - T/T_N)^{2\beta}$ of the intensities near T_N (dashed red curve).

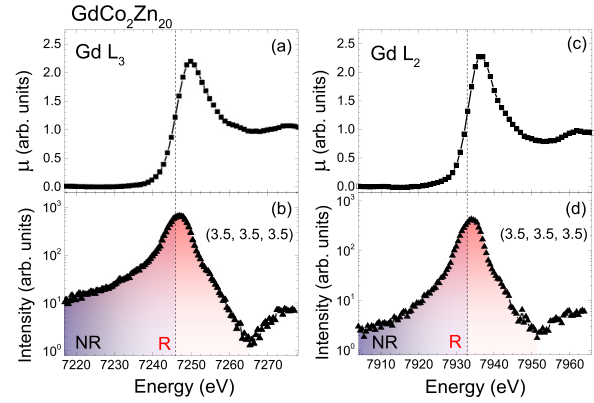


FIG. 7. Energy dependences obtained across the Gd L_3 and L_2 edges at 4.5 K of the absorption coefficients obtained from the fluorescence measurements in (a), (c) respectively and for the intensity of the superlattice peak $(\frac{7}{2}, \frac{7}{2}, \frac{7}{2})$ in the $\sigma - \pi'$ polarization channel in (b), (d) respectively. The vertical dashed lines correspond to the position of the absorption edge inflection. NR and R stand for nonresonant and resonant sections in (b) and (d).

addition, the maximum intensities are observed about 2–3 eV above the absorption edge (defined by the vertical dashed lines), which is a characteristic signature of a dipole electronic transition. The same energy dependence was performed in the $\sigma - \sigma'$ polarization channel and no significant contribution was observed. The strong resonant enhancement in the spectra [Figs. 7(b) and 7(d)] indicates a significant overlap between the initial $2p$ and $5d$ states, and a strong exchange interaction between the $4f - 5d$ orbitals. This magnetic polarization of the $5d$ bands via $4f$ states helps shed light on the magnetic structures of these rare-earth-based materials using the L absorption edge measurements, i.e., $2p \rightarrow 5d$ transitions. Moreover, the asymmetric peak shape expressed as a long tail below the absorption edges arises from the interference between the resonant and nonresonant magnetic scattering contributions [28–30].

The normalized energy line-shape dependence after absorption correction for selected magnetic Bragg peaks $(\frac{L}{2}, \frac{L}{2}, \frac{L}{2})$ with $L = (2n + 1)$ performed at Gd L_2 and L_3 edges is displayed in Fig. 8. The magnetic reflections show a narrow resonant line shape at the L_2 ($w \leq 4.9$ eV) and L_3 ($w \leq 5.9$ eV) edges. The smaller energy broadening for the L_2 edge is associated with a relatively short lifetime compared with the L_3 edge. The integrated intensities of the magnetic reflections were used to extract the L_3/L_2 ratio and to determine the direction of the magnetic moment. The BR values show an unusual behavior in which the values varies between 0.9–1.2 for different magnetic reflections. For XRMS, the branching ratio is expected to be equal to 1. The exact value for the BR ratio is difficult to obtain due to the various corrections that must be applied to the experimental data, such as self-absorption and angular corrections, and therefore we cannot affirm that $\langle L_z^{5d} \rangle \neq 0$ for this AFM compound.

C. Magnetic structure of GdCo₂Zn₂₀

The magnetic structure of the Gd spins is determined comparing the experimental integrated intensities in Fig. 8 with

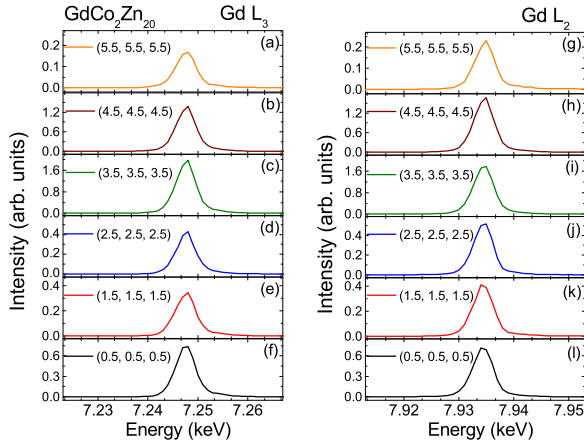


FIG. 8. Energy dependence of the x-ray resonant magnetic scattering intensities measured in the $\sigma - \pi'$ polarization channel for magnetic Bragg peaks of type $(\frac{L}{2}, \frac{L}{2}, \frac{L}{2})$ with $L = (2n + 1)$ after absorption correction. (a)–(f): at the Gd L_3 -absorption edge; (g)–(l): at the Gd L_2 edge.

simulated data from selected magnetic reflections. The SARAH [31] and ISODISTORT [32] softwares were used to determine the possible magnetic arrangements that the Gd ions can adopt inside the unit cell, i.e., the magnetic representation (Γ_{Mag}) and its magnetic space group. In addition, we assumed that only the Gd ions carry magnetic moments in this compound. For this material, whose magnetic propagation vector is $(\frac{1}{2}, \frac{1}{2}, \frac{1}{2})$ (point L in the Brillouin zone), whose space group is $Fd\bar{3}m$, and whose Gd ions occupy the $8a$ crystallographic site, the magnetic representation (MR) can be decomposed into four nonzero irreducible representations (irreps): two one-dimensional (1D $\Gamma_{2,3}$) and two two-dimensional (2D $\Gamma_{5,6}$) ones. The four possible magnetic representations for the AFM GdCo₂Zn₂₀ compound are summarized in Table I with their respective basis vectors (BVs). The propagation vector and the

TABLE I. Basis vectors (BVs) for the space group $Fd\bar{3}m:2$ with $\mathbf{k}_9 = (\frac{1}{2}, \frac{1}{2}, \frac{1}{2})$. The decomposition of the magnetic representation (MR) for the Gd site can be written as $\Gamma_{\text{Mag}} = \Gamma_2 + \Gamma_3 + \Gamma_5 + \Gamma_6$. The two rare-earth atoms' positions of the nonprimitive basis are defined according to 1: (0.125, 0.125, 0.125) and 2: (0.875, 0.875, 0.875).

IR	BV	Atom	BV components					
			$m_{\parallel a}$	$m_{\parallel b}$	$m_{\parallel c}$	$im_{\parallel a}$	$im_{\parallel b}$	$im_{\parallel c}$
Γ_2	ψ_1	1	1	1	1	0	0	0
		2	1	1	1	0	0	0
Γ_3	ψ_2	1	1	1	1	0	0	0
		2	-1	-1	-1	0	0	0
Γ_5	ψ_3	1	1/2	1/2	-1	0	0	0
		2	-1/2	-1/2	1	0	0	0
	ψ_4	1	0.866	-0.866	0	0	0	0
		2	-0.866	0.866	0	0	0	0
Γ_6	ψ_5	1	1/2	1/2	-1	0	0	0
		2	1/2	1/2	-1	0	0	0
	ψ_6	1	-0.866	0.866	0	0	0	0
		2	-0.866	0.866	0	0	0	0

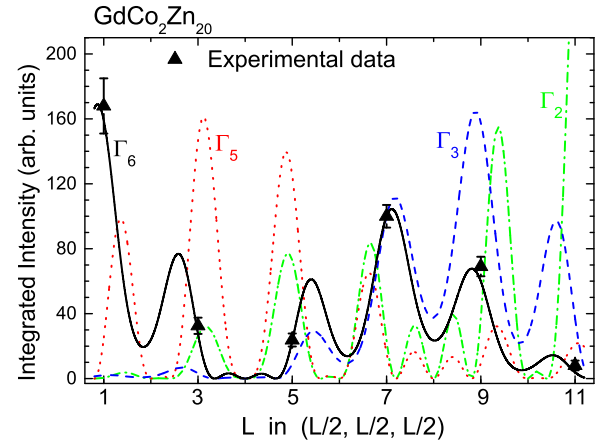


FIG. 9. Simulated and experimental integrated intensities for magnetic reflections $(\frac{L}{2}, \frac{L}{2}, \frac{L}{2})$ with $L = (2n + 1)$ performed at the Gd L_2 absorption edge for GdCo₂Zn₂₀. The simulated intensities were obtained through Eq. (1) supposing the four magnetic representations Γ_2 , Γ_3 , Γ_5 , and Γ_6 summarized in Table I. The error bars for the experimental data were extracted from the fitting function.

irreps are labeled following the Kovalev notation [33] as given by the program SARAH.

To determine the magnetic structure, the intensities were calculated assuming only dipole transition (E1) and, hence, the x-ray magnetic scattering cross-section model can be written as follows [17,34–38]:

$$I_{\text{RES}} \propto A * \left| \sum_n f_n^{E1} e^{i\vec{Q} \cdot \vec{R}_n} \right|^2, \quad (1)$$

where

$$A = \frac{\sin(\theta + \alpha) \sin(\theta - \alpha)}{\sin \theta \cos \alpha \sin(2\theta)}, \quad (2)$$

and

$$f_n^{E1} = [(\hat{\epsilon}' \cdot \hat{\epsilon})F^{(0)} - i(\hat{\epsilon}' \times \hat{\epsilon}) \cdot \hat{z}_n F^{(1)} + (\hat{\epsilon}' \cdot \hat{z}_n)(\hat{\epsilon} \cdot \hat{z}_n)F^{(2)}]. \quad (3)$$

The term A [Eq. (2)] contains the absorption correction and the Lorentz factor. α is the angle between the wave-vector transfer $\vec{Q} (= \vec{k}' - \vec{k})$ and the [111] crystal direction, and θ is half of the 2θ scattering angle. Equation (3) shows the resonant term. It carries information about the \vec{k} ($\hat{\epsilon}$) and \vec{k}' ($\hat{\epsilon}'$), i.e., the incident and scattered wave (polarization) vectors, respectively, and the magnetic moment direction at the n th site (\hat{z}_n). The terms $F^{(0,1,2)}$ are related to the dipole matrix transition and by atomic properties [38]. The exponential function in Eq. (1) is a function of the wave-vector transfer \vec{Q} , and the position \vec{R}_n of the n th Gd ion inside the unit cell. For the XRMS technique probing AFM materials, the magnetic intensity at the first harmonic satellites comes from the linear term on magnetic moment direction: $[-i(\hat{\epsilon}' \times \hat{\epsilon}) \cdot \hat{z}_n]$ displayed in Eq. (3).

The simulated intensities obtained using Eq. (1) and the experimental intensities obtained at the Gd L_2 edge [Figs. 7(g)–7(l)] are displayed in Fig. 9. The two irreps ($\Gamma_{2,3}$) show only one basis vector each (ψ_1 and ψ_2 , respectively).

Both irreps imply the magnetic spin moments aligned along the $[1,1,1]$ crystallographic direction. On the other hand, for the Γ_5 and Γ_6 irreps, the magnetic moment can be written as a linear combination of the BVs ψ_3 and ψ_4 for Γ_5 , and ψ_5 and ψ_6 for Γ_6 , i.e., $\mathbf{z}_n = c_{3,n}\psi_3 + c_{4,n}\psi_4$ or $\mathbf{z}_n = c_{5,n}\psi_5 + c_{6,n}\psi_6$, with c_{3-6} real or complex numbers. As displayed in Fig. 9, the simulated intensities regarding the Gd spins' moment directions were performed for different magnetic representations. The better agreement (smaller χ^2 of 1.5) is achieved when the magnetic structure is defined by the representation Γ_6 with $c_5 = -0.24$ and $c_6 = 0.27$. Using this information and the ISODISTORT software, we could assign the $P_5\bar{1}$ magnetic space group to this magnetic configuration [39].

To identify different magnetic propagation vectors, such as $(0, \frac{1}{2}, \frac{1}{2})$ and $(0, 0, \frac{1}{2})$, a systematic search for commensurate and incommensurate magnetic reflections in the reciprocal space was performed below T_N . However, only magnetic Bragg reflections of the type $(\frac{1}{2}, \frac{1}{2}, \frac{1}{2})$ were observed. In addition, to probe a possible presence of AFM magnetic moments in the Co and Zn ions, the beam energy was tuned to the Co and Zn K edges and a search for magnetic superlattice reflections was performed below T_N . No measurable magnetic reflections at 4.5 K could be observed at those edges.

IV. DISCUSSION

The nature of the electronic and magnetic properties of the intermetallic RT_2Zn_{20} systems depends strongly on the interactions between the rare-earth and the transition-metal ions. Since the Gd $5d$ states participate on the conduction bands, the resonant absorption and diffraction measurements at the Gd $L_{2,3}$ edges provide valuable information. As reported in susceptibility measurements and band structure calculations [2,3], the replacement of the transition metal affects the electronic density of states at the Fermi level (ρ_{E_F}) and the conduction band without significantly changing the lattice parameters [40]. Doping studies of $Gd(Fe_xCo_{1-x})_2Zn_{20}$ compounds show a monotonic increase of the magnetic ordering temperature when x increases to 1, which indicates that there is an increase in the coupling between the rare-earth magnetic moments [2].

Absorption measurements performed in powdered samples of FM $GdFe_2Zn_{20}$ compound below T_C reveal interesting behaviors. As can be seen in Figs. 2–5, only at the Gd L and Zn K edges is a dichroic signal observed above the background level, while an unexpected lack of magnetic intensity is observed at the Fe K edge. The intense magnetic signal at the rare-earth L edges occurs mainly due to the overlap between the Gd $2p$ and $5d$ states and a strong energy splitting of the $5d$ subbands as a result of a $4f-5d$ exchange interaction [42–45]. In addition, the splitting of the d states into $5d$ spin-up and spin-down wave functions has considerable influence on the magnetism observed at the Zn K edge. The Zn $3d$ orbitals are completely filled ($3d^{10}$) and, henceforth, a magnetic moment due to an overlap between the $3d$ and $4sp$ orbitals in the Zn ion is not expected to occur due to the filled $3d$ orbitals being more contracted. Therefore, the magnetic signal observed in the $4p$ states is due to hybridization with the extended Gd $5d$ orbitals and not from the exchange interaction with the Zn $3d^{10}$ orbitals [18,25]. Following Hund's rule, the Gd ion has the $4f$ state filled by seven spin-up electrons in which it pulls the

$5d$ subband spin-up function towards the inner core due to a positive exchange interaction. The short distances between the first Gd-Zn ions ($\sim 3 \text{ \AA}$) drives a small hybridization between the broad Zn $4p$ and Gd $5d$ states, inducing a small amount of magnetic moment in the $4p$ states.

Theoretical studies have suggested that the orbital moment should be almost zero for the $5d$ band ($\langle L_z^{5d} \rangle = 0$), i.e., a quenching of the angular momentum, so the $5d_{3/2}$ and $5d_{5/2}$ subbands should display the same polarization, and thereby the dichroism at the L_3 and L_2 edges should have equal magnetic intensity [23,41,44]. For the $GdCo_2Zn_{20}$ compound, the BR ratio varies between 0.9–1.2, i.e., close to the theoretical value, and therefore we cannot suggest any orbital moment for this compound. However, as showed in Fig. 2 for the FM compound, the intensity recorded at the L_2 edge is higher than at the L_3 edge, where we observe a L_3/L_2 ratio of approximately $-0.77(4)$ [46]. This slightly different value from the theoretical branching ratio expected for XMCD (BR = -1) suggests that the Gd ions may carry a small orbital moment at the $5d$ orbitals in the FM compound.

Mössbauer spectroscopy measurements [47] and simulations [48] for the $DyFe_2Zn_{20}$ compound reported that the Fe ions align AFM with the Dy magnetic moments in which the iron ions exhibit a very small magnetic moment, $\sim 0.2 \mu_B/Fe$. Neutron-diffraction measurements [7] performed on $TbFe_2Zn_{20}$ also reported that a small magnetic moment at the Fe ions ($< 1 \mu_B$) would improve the refinement. In addition, recently, Mössbauer measurements [49] on $GdFe_2Zn_{20}$ also reported the presence of a small magnetic contribution at the Fe site. In order to verify the quality of our XMCD data at the Fe K edge, dichroic measurements at low temperature and under magnetic field in a $5 \mu m$ Fe foil was also carried out. A magnetic signal around 0.3% which, according to the literature [50,51], corresponds to a magnetic moment of around $2.2 \mu_B/Fe$ was observed. Assuming that the Fe spins order ferromagnetically in $GdFe_2Zn_{20}$ with a magnetic signal below 0.07% (noise level), it would result in a magnetic moment lower than $\mu_{Fe} \sim 0.5 \mu_B$, i.e., the same order of magnitude as reported by band structure calculations [2] and comparable with the $DyFe_2Zn_{20}$ compound. Therefore, if the Fe ions carry magnetic contribution in the $GdFe_2Zn_{20}$ materials, we can suggest that this magnetic moment must be lower than $0.5 \mu_B$. One possible explanation for the difficulty in identifying the magnetic signal at the Fe K edge (7112 eV) would be contamination coming from the Gd L_3 edge (7243 eV). Despite the fact that the two edges are apart by around 130 eV, the Gd L_3 pre-edge increases the background around the Fe K edge which, as a consequence, may hide the small magnetic signal. An AFM ordering state for the Fe ions cannot be ruled out for this compound; however, it is less likely to occur due to the FM alignment of the Gd ions.

Field-dependent magnetization measurements [2] show that the $GdFe_2Zn_{20}$ compound reaches a saturation magnetization of $6.5 \mu_B/f.u.$ at low temperature. Assuming that the Gd ions contribute with $7.94 \mu_B/Gd$ for the total magnetic moment (theoretical value) and that the transition metals are coupling antiferromagnetically with the rare-earth elements, the transition metals are found to carry a magnetic moment around $1.44 \mu_B/f.u.$ opposite to the Gd ions. If the Fe ions have a total magnetic moment $\mu_{Fe} \sim 0.5 \mu_B$, then consequently the Zn

ions present in this material would present an induced magnetic moment of approximately $0.05 \mu_B/\text{Zn}$. Therefore, it strongly suggests that the interaction between the rare-earth ions affects the environment around the atoms and consequently spin polarizes the transition-metal ion. The rough estimate of magnetic moment for the Zn ions based on spectroscopy and macroscopic measurements has to be further investigated.

To provide further information about these systems, the magnetic properties of the AFM compound $\text{GdCo}_2\text{Zn}_{20}$ were also investigated, using the XRMS technique. The transition to the magnetically ordered phase driven by temperature is characterized by the appearance of superlattice magnetic reflections with a magnetic propagation vector $\vec{\tau} = (\frac{1}{2}, \frac{1}{2}, \frac{1}{2})$. This $\vec{\tau}$ magnetic vector indicates that the magnetic unit cell is represented by a doubled chemical unit cell in all three crystallographic directions. In addition, as seen in Fig. 9, the experimental and simulated intensities regarding the Gd spins' moment directions were performed for different magnetic representations and the magnetic structure is identified as magnetic representation Γ_6 in which the magnetic moment can be written as a linear combination of the BVs ψ_5 and ψ_6 . For this magnetic structure, the magnetic space group is $P5\bar{1}$.

Since the closest distance between the rare-earth ions is $\sim 6 \text{ \AA}$, the magnetic properties in this system will be mainly mediated via the conduction electrons. This large distance explains quite well a weakening of the J_{RKKY} exchange interaction and thus a very low representative magnetic transition temperature, i.e., approximately 5.7 K ($\text{GdCo}_2\text{Zn}_{20}$) and 2.5 K ($\text{TbCo}_2\text{Zn}_{20}$). As a consequence of a poor J_{RKKY} coupling, the surrounding matrix around the R ions is weakly affected and hence it is not possible to induce a magnetic moment in the transition-metal ions. The absence of magnetism in the transition-metal ions is also observed in the $\text{TbCo}_2\text{Zn}_{20}$ compound [7]. For the Tb-based materials, the crystalline electric field (CEF) splitting can affect the J_{RKKY} constant and therefore influence the magnetic coupling and the transition temperature. It is well known that the CEF splitting induces magnetic anisotropies in the ground state and that it may influence the total angular momentum. Several Tb-based intermetallics have exhibited distinct magnetic properties in relation to the Gd counterparts, as shown in the layered family $R_n T_m M_{3n+2m}$ (R = rare earth; T and M = transition metal; $n = 1, 2$ and $m = 0, 1$) [52–54]. Although the $\text{GdCo}_2\text{Zn}_{20}$ and $\text{TbCo}_2\text{Zn}_{20}$ compounds display the same magnetic propagation vector $(\frac{1}{2}, \frac{1}{2}, \frac{1}{2})$, their magnetic structures are different, which is mainly related to the competition between the RKKY and CEF interactions. Jia *et al.* [4] evaluated the CEF parameters from the thermodynamic measurements for the entirely $\text{RCO}_2\text{Zn}_{20}$ series ($R = \text{Tb-Tm}$) and they observe small energy scales and a large B_6^0 CEF parameter for the complete series. This finding suggests a small energy level splitting and a strong influence of the Zn cage on the rare-earth ions, i.e., guest-framework interaction. Therefore, we suggest that the rare-earth ions located in

this large polarized environment are strongly affected by the Zn cages, which has a direct influence on the electronic and magnetic properties. This can be seen in the different magnetic structures for the AFM compounds and the spin polarization of the Zn ions only for the $\text{GdFe}_2\text{Zn}_{20}$ compound. Hence, the CEF effect has an important role in this class of compound. A detailed investigation for different rare-earth elements would allow a better understanding of the $\text{RCO}_2\text{Zn}_{20}$ family. Nevertheless, macroscopic measurements down to 1.8 K report a magnetic ordering only for the compounds with $R = \text{Gd}$ and Tb .

V. SUMMARY

We have investigated the intermetallic $\text{GdT}_2\text{Zn}_{20}$ system with $T = \text{Co}$ and Fe at low temperature using the XRMS and XANES/XMCD techniques, respectively. The XRMS measurements performed in $\text{GdCo}_2\text{Zn}_{20}$ compound reveal a commensurate antiferromagnetic ordering with a magnetic propagation vector $(\frac{1}{2}, \frac{1}{2}, \frac{1}{2})$ in which only the Gd ions carry magnetic moments. Selected magnetic reflections were measured in the polarization channel $\sigma - \pi'$ and we identified that the Gd spins follow the magnetic representation Γ_6 , which is different from the isostructural compound $\text{TbCo}_2\text{Zn}_{20}$, mainly due to the CEF effects in the latter. The evolution of the magnetic signal showed a magnetic phase transition below $T_N = 5.72(6) \text{ K}$ with a critical exponent $\beta = 0.36(3)$, suggesting a three-dimensional (3D) Heisenberg magnetic model. The XANES and XMCD measurements performed at the Gd $L_{2,3}$ edges in $\text{GdFe}_2\text{Zn}_{20}$ reveal a strong magnetic signal ($\sim 12.5\%$ for L_2 and 9.7% for L_3), indicating a splitting of the $5d$ orbitals and a strong Gd-Gd exchange interaction as well as a nonzero orbital moment. In addition, we observe the presence of a small magnetic dichroic signal at the Zn K edge due to the spin polarization of the Gd $5d$ orbitals. This indicates a large RKKY exchange interaction between the Gd-Gd ions, which polarizes the surrounding matrix.

ACKNOWLEDGMENTS

This work was supported by FAPESP (SP-Brazil) under Contracts No. 2009/10264-0, No. 2011/19924-2, No. 2011/24166-0, No. 2012/10675-2, and No. 2012/17562-9. Parts of this research were carried out at the light source PETRA III at DESY, a member of the Helmholtz Association (HGF). Work at Argonne National Laboratory is supported by the U.S. Department of Energy, Office of Science, Office of Basic Energy Sciences, under Contract No. DE-AC-02-06CH11357. We would like to thank R. D. Reis and C. S. B. Dias for their assistance in macroscopic measurements and J. W. Kim for his assistance at beam line 6-ID-B. We are indebted to D. Reuther, R. Kirchhof, and H.-C. Wille for their assistance with the electromagnet at P09/DESY.

[1] M. S. Torikachvili, S. Jia, E. D. Mun, S. T. Hannahs, R. C. Black, W. K. Neils, D. Martien, S. L. Bud'ko, and

P. C. Canfield, *Proc. Natl. Acad. Sci. USA* **104**, 9960 (2007).

- [2] S. Jia, S. L. Bud'ko, G. D. Samolyuk, and P. C. Canfield, *Nat. Phys.* **3**, 334 (2007).
- [3] S. Jia, Ni Ni, G. D. Samolyuk, A. Safa-Sefat, K. Dennis, Hyunjin Ko, G. J. Miller, S. L. Bud'ko, and P. C. Canfield, *Phys. Rev. B* **77**, 104408 (2008).
- [4] S. Jia, Ni Ni, S. L. Bud'ko, and P. C. Canfield, *Phys. Rev. B* **80**, 104403 (2009).
- [5] T. Onimaru, K. T. Matsumoto, Y. F. Inoue, K. Umeo, Y. Saiga, Y. Matsushita, R. Tamura, K. Nishimoto, I. Ishii, T. Suzuki, and T. Takabatake, *J. Phys. Soc. Jpn.* **79**, 033704 (2010).
- [6] T. Nasch, W. Jeitschko, and U. C. Rodewald, *Z. Naturforsch., B: Chem. Sci.* **52**, 1023 (1997).
- [7] W. Tian, A. D. Christianson, J. L. Zarestky, S. Jia, S. L. Bud'ko, P. C. Canfield, P. M. B. Piccoli, and A. J. Schultz, *Phys. Rev. B* **81**, 144409 (2010).
- [8] N. Ni, S. Jia, G. D. Samolyuk, A. Kracher, A. S. Sefat, S. L. Bud'ko, and P. C. Canfield, *Phys. Rev. B* **83**, 054416 (2011).
- [9] D. Yazici, B. D. White, P.-C. Ho, N. Kanchanavatee, K. Huang, A. J. Friedman, A. S. Wong, V. W. Burnett, N. R. Dilley, and M. B. Maple, *Phys. Rev. B* **90**, 144406 (2014).
- [10] P. C. Canfield and Z. Fisk, *Philos. Mag.* **65**, 1117 (1992).
- [11] R. A. Ribeiro and M. A. Avila, *Philos. Mag.* **92**, 2492 (2012).
- [12] J. W. Freeland, J. C. Lang, G. Srajer, R. Winarski, D. Shu, and D. M. Mills, *Rev. Sci. Instrum.* **73**, 1408 (2002).
- [13] J. Strempler, S. Francoual, D. Reuther, D. K. Shukla, A. Skaugen, H. Schulte-Schrepping, T. Kracht, and H. Franz, *J. Synchrotron Radiat.* **20**, 541 (2013).
- [14] K. Hirano, K. Izumi, T. Ishikawa, S. Annaka, and S. Kikuta, *Jpn. J. Appl. Phys.* **30**, L407 (1991).
- [15] S. Francoual, J. Strempler, D. Reuther, D. K. Shukla, and A. Skaugen, *J. Phys.: Conf. Ser.* **425**, 132010 (2013).
- [16] J. C. Lang and G. Srajer, *Rev. Sci. Instrum.* **66**, 1540 (1995).
- [17] J. Hill and D. McMorrow, *Acta Crystallogr. A* **52**, 236 (1996).
- [18] R.-M. Galéra, Y. Joly, A. Rogalev, and N. Binggeli, *J. Phys.: Condens. Matter* **20**, 395217 (2008).
- [19] B. T. Thole and G. van der Laan, *Phys. Rev. B* **38**, 3158 (1988).
- [20] G. van der Laan and B. T. Thole, *Phys. Rev. B* **42**, 6670 (1990).
- [21] G. van der Laan and B. T. Thole, *Phys. Rev. B* **43**, 13401 (1991).
- [22] G. van der Laan, *Phys. Scr.* **41**, 574 (1990).
- [23] M. van Veenendaal, J. B. Goedkoop, and B. T. Thole, *Phys. Rev. Lett.* **78**, 1162 (1997).
- [24] V. N. Antonov, B. N. Harmon, A. N. Yaresko, and A. P. Shpak, *Phys. Rev. B* **75**, 184422 (2007).
- [25] J. P. Rueff, R. M. Galéra, Ch. Giorgetti, E. Dartyge, Ch. Brouder, and M. Alouani, *Phys. Rev. B* **58**, 12271 (1998).
- [26] M. F. Collins, *Magnetic Critical Scattering* (Oxford University Press, Oxford, 1989).
- [27] S. Blundell, *Magnetism in Condensed Matter*, Oxford Master Series in Condensed Matter Physics (Oxford University Press, Oxford, 2001).
- [28] D. Gibbs, G. Grübel, D. R. Harshman, E. D. Isaacs, D. B. McWhan, D. Mills, and C. Vettier, *Phys. Rev. B* **43**, 5663 (1991).
- [29] J. W. Kim, Y. Lee, D. Wermeille, B. Sieve, L. Tan, S. L. Bud'ko, S. Law, P. C. Canfield, B. N. Harmon, and A. I. Goldman, *Phys. Rev. B* **72**, 064403 (2005).
- [30] M. G. Kim, A. Kreyssig, Y. B. Lee, R. J. McQueeney, B. N. Harmon, and A. I. Goldman, *Eur. Phys. J. Spec. Top.* **208**, 157 (2012).
- [31] A. S. Wills, *Physica B* **276–278**, 680 (2000).
- [32] B. J. Campbell, H. T. Stokes, D. E. Tanner, and D. M. Hatch, *J. Appl. Crystallogr.* **39**, 607 (2006).
- [33] O. V. Kovalev, *Representations of the Crystallographic Space Groups*, 2nd ed., edited by H. T. Stokes and D. M. Hatch (Gordon and Breach Science, Yverdon, Switzerland, 1993).
- [34] C. Detlefs, A. H. M. Z. Islam, A. I. Goldman, C. Stassis, P. C. Canfield, J. P. Hill, and D. Gibbs, *Phys. Rev. B* **55**, R680(R) (1997).
- [35] C. Adriano, R. Lora-Serrano, C. Giles, F. de Bergevin, J. C. Lang, G. Srajer, C. Mazzoli, L. Paolasini, and P. G. Pagliuso, *Phys. Rev. B* **76**, 104515 (2007).
- [36] S. Nandi, Y. Su, Y. Xiao, S. Price, X. F. Wang, X. H. Chen, J. Herrero-Martín, C. Mazzoli, H. C. Walker, L. Paolasini, S. Francoual, D. K. Shukla, J. Strempler, T. Chatterji, C. M. N. Kumar, R. Mittal, H. M. Rønnow, Ch. Rüegg, D. F. McMorrow, and Th. Brückel, *Phys. Rev. B* **84**, 054419 (2011).
- [37] J. R. L. Mardegan, C. Adriano, R. F. C. Vescovi, G. A. Faria, P. G. Pagliuso, and C. Giles, *Phys. Rev. B* **89**, 115103 (2014).
- [38] J. P. Hannon, G. T. Trammell, M. Blume, and D. Gibbs, *Phys. Rev. Lett.* **61**, 1245 (1988).
- [39] J. M. Perez-Mato, S. V. Gallego, E. S. Tasci, L. Elcoro, G. de la Flor, and M. I. Aroyo, *Annu. Rev. Mater. Res.* **45**, 217 (2015).
- [40] The GdFe₂Zn₂₀ compound has a cubic lattice parameter a around 0.07 Å larger than GdCo₂Zn₂₀; hence, a modification in the unit cell volume of ~3% by replacing the ion.
- [41] M. Imada, A. Fujimori, and Y. Tokura, *Rev. Mod. Phys.* **70**, 1039 (1998).
- [42] J. Osterwalder, in *Magnetism: A Synchrotron Radiation Approach*, Lecture Notes in Physics, edited by Eric Beaurepaire (Springer, New York, 2006).
- [43] H. König, X. Wang, B. N. Harmon, and P. Carra, *J. Appl. Phys.* **76**, 6474 (1994).
- [44] B. N. Harmon and A. J. Freeman, *Phys. Rev. B* **10**, 1979 (1974).
- [45] B. N. Harmon and A. J. Freeman, *Phys. Rev. B* **10**, 4849 (1974).
- [46] The minus sign arising from the spin-orbit interaction in the initial $2p$ state.
- [47] I. Tamura, Y. Isikawa, T. Mizushima, and S. Miyamoto, *J. Phys. Soc. Jpn.* **82**, 114703 (2013).
- [48] Y. Isikawa, T. Mizushima, S. Miyamoto, K. Kumagai, M. Nakahara, H. Okuyama, T. Tayama, T. Kuwai, and P. Lejay, *J. Korean Phys. Soc.* **63**, 644 (2013).
- [49] S. L. Bud'ko, T. Kong, X. Ma, and P. C. Canfield, *J. Phys.: Condens. Matter* **27**, 336003 (2015).
- [50] S. Stahler, G. Schutz, and H. Ebert, *Phys. Rev. B* **47**, 818 (1993).
- [51] V. Iota, J.-H. P. Klepeis, C.-S. Yoo, J. Lang, D. Haskel, and G. Srajer, *Appl. Phys. Lett.* **90**, 042505 (2007).
- [52] J. D. Thompson and Z. Fisk, *J. Phys. Soc. Jpn.* **81**, 011002 (2012), and references therein.
- [53] J. D. Thompson, R. Movshovich, Z. Fisk, F. Bouquet, N. J. Curro, R. A. Fisher, P. C. Hammel, H. Hegger, M. F. Hundley, M. Jaime, P. G. Pagliuso, C. Petrovic, N. E. Phillips, and J. L. Sarrao, *J. Magn. Magn. Mater.* **226–230**, 5 (2001).
- [54] R. Flint, M. Dzero, and P. Coleman, *Nat. Phys.* **4**, 643 (2008).